

Baryonic dense matter in view of gravitational-wave observations

Vivek Baruah Thapa^{*}, Anil Kumar[†] and Monika Sinha[‡]

Indian Institute of Technology Jodhpur, Jodhpur 342037, India

15 January 2022

ABSTRACT

The detection of gravitational waves from the merger of binary neutron stars events (GW170817, GW190425) and subsequent estimations of tidal deformability play a key role in constraining the behaviour of dense matter. In addition, massive neutron star candidates ($\sim 2M_{\odot}$) along with NICER mass-radius measurements also, set sturdy constraints on the dense matter equation of state. Strict bounds from gravitational waves and massive neutron stars observations constrain the theoretical models of nuclear matter compartment at large density regimes. On the other hand, model parameters providing the highly dense matter response are bounded by nuclear saturation properties. This work analyses coupling parametrizations from two classes based on covariant density functional models: Non-Linear and Density-Dependent schemes. Considering these constraints together, we study possible models and parametrization schemes with the feasibility of exotic degrees of freedom in dense matter which go well with the astrophysical observations as well as the terrestrial laboratory experiments. We show that most parametrizations with non-linear schemes do not support the observations and experiments while density-dependent scheme goes well with both. Astrophysical observations are well explained if the inclusion of heavier non-strange baryons is considered as one fraction of the dense matter particle spectrum.

Key words: stars: neutron; equation of state; dense matter; gravitational waves

1 INTRODUCTION

Neutron stars (NSs), one of the most compact objects in the universe, provide a suitable environment to study matter at densities ranging from sub-saturation to few times nuclear saturation densities (Glendenning 1996; Sedrakian 2007; Weber 2017). The well-known strategy to comprehend dense matter behaviour above nuclear saturation density (n_0) is understanding compact astrophysical objects. Constraints from observation of compact stellar objects help the understanding of dense matter above n_0 . One important constraint is the lower limit of maximum stellar mass of compact object family obtained from several recent observations. On the high density regime, the primary constraint on equation of state (EOS) comes from the observations of massive compact stars with masses near $2M_{\odot}$. Observations of massive compact objects constrain the EOS to be stiff at a higher density limit. In addition, the recent NICER (Neutron star Interior Composition Explorer) observations provide the mass and radius measurements of two compact objects (PSR J0030 + 0451, PSR J0740 + 6620), which further constrain the EOS.

Massive compact star observations eradicate the softer EOSs failing to support the observational lower bound on maximum mass stars. On the other hand, the recent detection of gravitational waves (GWs) emissions from binary neutron star (BNS) inspiral of the event GW170817 (Abbott et al. 2017a,b,c) and GW190425 (Abbott et al. 2020a) by LIGO-Virgo Collaboration (LVC) imposes bounds (although weakly) on intermediate densities of dense matter EOS. In

the BNS merger scenario, the response of a compact star to a strong gravitational field exerted by its companion is related to the EOS via induced tidal deformations during the inspiral phase. Recent observations of gravitational wave (GW) from binary star coalescence directly provide the estimate of combined dimensionless tidal deformability ($\bar{\Lambda}$) of participating stars indicating matter to be soft at a lower density regime.

Due to insufficient knowledge and restrictions about matter properties at density regimes higher than n_0 , it is tough and challenging to predict the behaviour of dense matter. Several studies have been done to comprehend the NS matter composition in phenomenological (Vautherin & Brink 1972; Douchin & Haensel 2001; Bao & Shen 2014) as well as microscopic approaches (Akmal et al. 1998; Carlson et al. 2015; Logoteta 2019). Phenomenological models such as the Relativistic Mean-Field (RMF) model (Walecka 1974; Boguta & Bodmer 1977; Serot & Walecka 1997) based on effective interactions between baryons via meson exchange can conveniently describe various finite nuclei properties and can be extrapolated from sub-saturation to higher density regimes (Lattimer & Prakash 2016). Within this framework, there are a good number of admissible phenomenological models, each with a good number of parameter values sets. With recent observational constraints related to compact stars it is possible to narrow down the models of dense matter EOS.

Observations of massive NSs open the likelihood of exotic matter such as hyperons (Glendenning & Moszkowski 1991a; Weissenborn et al. 2012; Bonanno & Sedrakian 2012; Colucci & Sedrakian 2013; Oertel et al. 2015; Fortin et al. 2016; Tolos et al. 2017; Raduta et al. 2018; Li et al. 2018a), Δ -resonances (Drago et al. 2014; Cai et al. 2015; Zhu et al. 2016; Sahoo et al. 2018; Kolomeitsev et al. 2017; Li et al. 2018c; Li & Sedrakian 2019; Ribes et al. 2019;

^{*} thapa.l@iitj.ac.in

[†] anil.1@iitj.ac.in

[‡] ms@iitj.ac.in

Li et al. 2020a; Thapa et al. 2020), meson (π, \bar{K}, ρ -mesons) condensations (Mannarelli 2019; Haensel & Proszynski 1982; Glendenning & Schaffner-Bielich 1999; Banik & Bandyopadhyay 2001; Prakash et al. 1997; Malik et al. 2021; Thapa & Sinha 2020; Thapa et al. 2021)) in the NS interior details of which are still not completely understood. Although hyperonization in NSs may seem to be inescapable, it leads to softening of the EOS. Following similar energetic reasoning employed for nucleation of strange baryons, another interesting aspect is the onset of non-strange Δ -baryons in dense NS matter. The role of Δ -resonances in NS matter is still a matter of debate (Li et al. 2018b; Motta et al. 2020). Inclusion of Δ -baryons softens the EOS at lower matter density regimes leading to higher compactness at those densities, consequently satisfying the GW170817 event observables (Li & Sedrakian 2019). Similar to other exotic degrees of freedom, the inclusion of meson condensates also softens the EOS extensively. For recent reviews regarding the composition of compact stars, the reader may refer to Refs.-Yagi & Yunes (2017); Chatterjee & Vidaña (2016); Sedrakian, Armen (2017); Baym et al. (2018); Sedrakian et al. (2021).

In our present work, we employ the available constraints obtained so far from compact objects observations to narrow down the high-density matter models. We explore the possible parameterization models based on constraints from terrestrial experiments and astrophysical observations (viz. massive NSs, radii estimations of NSs, GW emitted during the inspiral phase of BNS coalescence) on dense matter EOS. To construct the EOS, we consider non-linear Walecka (NLW) type and density-dependent (DD) meson-baryon couplings within covariant density Functional (CDF) model with exotic degrees of freedom in addition to nucleons. The phenomenological EOS models based on density functional theories and realistic nuclear potentials have been analyzed considering matter composition to be only nucleonic (Malik et al. 2018; Nandi et al. 2019; Kanakis-Pegios & Moustakidis 2020). Therefore, this work will explore the novel aspects of CDF model parametrizations that satisfy the recent astrophysical observable estimations considering hyperonization of dense matter to be a viable energetic argument.

The paper is organized as follows. In sec.2, we describe a few estimated parameters of compact stellar objects from observational constraints relevant to our present work. The CDF model formalism (NLW and DD), its extension to heavier baryons in β -equilibrated nuclear matter, aspects of tidal deformability of NSs and coupling parameters incorporated in this work are described in sec. 3. Sec.-4 provides the results and our conclusions and future perspectives are summarized in sec.-5.

Conventions: We implement the natural units $G = \hbar = c = 1$ throughout the work.

2 OBSERVATIONAL CONSTRAINTS

The understanding of dense matter above n_0 can be reasonably improved from recent compact stars observations as the constraints on lower limit of maximum mass, observed range of mass-radius of certain compact stars and most importantly the compactness from observed tidal deformability. The soft EOS of highly dense matter can be ruled out from the observations of massive stars viz. PSR J1614–2230 ($M = 1.908 \pm 0.016 M_\odot$) (Demorest et al. 2010; Arzoumanian et al. 2018), PSR J0348+0432 ($2.01 \pm 0.04 M_\odot$) (Antoniadis et al. 2013), millisecond pulsar (MSP) J0740 + 6620 ($2.14^{+0.20}_{-0.18} M_\odot$ with 95% credibility (Cromartie et al. 2020), $2.08^{+0.07}_{-0.07} M_\odot$ with 68.3% credibility (Fonseca et al. 2021)) and PSR J1810 + 1744 ($2.13 \pm 0.04 M_\odot$ with 68% credibility) (Romani et al. 2021).

GW observations also can constrain well the models of highly dense matter as already stated. For low-spin prior systems from GW170817 event, it is estimated that the combined dimensionless tidal deformability ($\tilde{\Lambda}$) parameter value has an upper and lower bounds of 900 (TaylorF2 model) (Abbott et al. 2017a) and 400 (AT2017gfo event) (Radice et al. 2018) respectively. Re-analysis of the GW170817 data by LVC has set new limits as $110 \leq \tilde{\Lambda} \leq 720$ (PhenomPNRT model) (Abbott et al. 2019). Another estimation of $\tilde{\Lambda}$ based on the viability of chiral effective field theory results provides the limit to be in the range $80 \leq \tilde{\Lambda} \leq 570$ (Tews et al. 2018). In addition, an ameliorated analysis of GW170817 event data implementing identical EOS for both the compact stars producing rational waveforms provides a limit on the dimensionless tidal deformability (Λ) for a $1.4M_\odot$ NS to be in the range $70 \leq \Lambda_{1.4} \leq 580$ with 90% credibility (Abbott et al. 2018). Raithel et al. (2018) reported that the $\tilde{\Lambda} \leq 800$ constraint implies the radius of primary compact object to be < 13 km.

Another GW observation (GW190814) by the LIGO Livingston detector (LVC) inferred to be from a coalescence of a black-hole (BH) and lighter compact object appendage with mass of the latter to be $2.59^{+0.08}_{-0.09} M_\odot$ (Abbott et al. 2020b) which falls in the ‘mass-gap’. The nature of lighter companion is still not resolved (Most et al. 2020; Tews et al. 2021; Sedrakian et al. 2020; Li et al. 2020b; Dexheimer et al. 2021; Bombaci et al. 2020; Fattoyev et al. 2020).

Along with this, we get good information about mass-radius relation of compact stars from NICER observations. This space mission recently provided adequate information to estimate the mass-radius of PSR J0030 + 0451 to be in the range of $1.44^{+0.15}_{-0.14} M_\odot$, $13.02^{+1.24}_{-1.06}$ km (Miller et al. 2019) and $1.34^{+0.15}_{-0.16} M_\odot$, $12.71^{+1.14}_{-1.19}$ km (with 68.3% credibility) (Riley et al. 2019) respectively. Latest estimate of mass-radius of PSR J0740 + 6620 by NICER is in the range of $2.072^{+0.067}_{-0.066} M_\odot$, $12.39^{+1.30}_{-0.98}$ km (Riley et al. 2021) and $2.08 \pm 0.07 M_\odot$, $13.71^{+2.62}_{-1.50}$ km (with 68% credibility) (Miller et al. 2021) respectively. Several works (Zhang & Li 2021; Biswas 2021; Pang et al. 2021; Raaijmakers et al. 2021; Somasundaram & Margueron 2021; Li et al. 2021a) have been performed based on different analyses on astrophysical observations inclusive of the latest NICER measurements to extract new information regarding dense matter EOS.

An estimation for tidal deformability from NICER observations of PSR J0030 + 0451 jointly with GW170817 event provides $240 \leq \Lambda_{1.4} \leq 730$ with radius range as $R_{1.4} = 12.1^{+1.2}_{-0.8}$ km (Jiang et al. 2020). Another recent analysis of the same PSR J0030 + 0451 data (NICER) reveals $R_{1.4} = 12.32^{+1.09}_{-1.47}$ km (Landry et al. 2020). The radius constraint on the $1.4M_\odot$ NSs from the GW170817 event has been derived to be in the range $10.5 \leq R_{1.4}/\text{km} \leq 13.4$ (Abbott et al. 2019) while Malik et al. (2018) provides the radius limit to be $11.82 \leq R_{1.4}/\text{km} \leq 13.72$. Considering similar low-spin prior systems for the GW190425 event, an upper bound of 600 (PhenomPv2NRT model) has been placed on $\tilde{\Lambda}$ and the radius upper limit is derived as $R < 15$ km (Abbott et al. 2020a).

From the analysis of GW170817 event data, bounds on matter pressure ranges are derived at $2n_0$ and $6n_0$ to be $3.5^{+2.7}_{-1.7} \times 10^{34}$ dyn/cm² and $9.0^{+7.9}_{-2.6} \times 10^{35}$ dyn/cm² respectively (Abbott et al. 2018). Recent results obtained from GW170817 event by Bayesian analysis suggest matter pressure at $2n_0$ to be $\sim 3.81^{+1.18}_{-2.32} \times 10^{34}$ dyn/cm² and $133 \leq \Lambda_{1.4} \leq 686$ (Li et al. 2021b). The analysis of GW190425 event data reveals core matter density of the primary component involved to be in the range $3 \leq n/n_0 \leq 6$ and matter pressure to be in $10^{35} \leq P(3 - 6 n_0) \leq 8 \times 10^{35}$ dyn/cm² range (Abbott et al. 2020a).

We take into consideration the source properties at 90% credible

intervals with low-spin posterior distributions from PhenomPNRT (Abbott et al. 2019) and PhenomPv2NRT (Abbott et al. 2020a) waveform models for GW170817 and GW190425 respectively to evaluate various GW observables. Based on recent observable estimations of GW events, in addition to setting radius bounds on the NSs involved in GW170817 and GW190425 events, we also find limits on compactness parameter for a $1.4 M_\odot$ NS.

3 FORMALISM

3.1 EOS Model

In this section, we briefly discuss the NLW and DD CDF models implemented to contrive the EOS in this work. The dense matter possible constituents considered here are nucleons ($N \equiv n, p$), hyperons ($Y \equiv \Lambda^0, \Sigma^{\pm,0}, \Xi^{-,0}$) and Δ -resonances ($\Delta \equiv \Delta^{++}, \Delta^+, \Delta^-, \Delta^0$) alongside leptons ($l \equiv e^-, \mu^-$) to maintain β -equilibrium. The interaction between non-strange baryons are described via the exchange of isoscalar-scalar σ , isoscalar-vector ω and isovector-vector ρ mesons. For the hyperonic sector interactions, an additional hidden strangeness isoscalar-vector ϕ meson is taken into consideration. In general, the total Lagrangian density describing the baryon-meson interactions is given by (Glendenning & Schaffner-Bielich 1999; Banik & Bandyopadhyay 2001; Li et al. 2018c)

$$\begin{aligned} \mathcal{L} = & \sum_{b \equiv N, Y} \bar{\psi}_b (i\gamma_\mu D_{(b)}^\mu - m_b^*) \psi_b + \sum_l \bar{\psi}_l (i\gamma_\mu \partial^\mu - m_l) \psi_l \\ & + \sum_\Delta \bar{\psi}_{\Delta\nu} (i\gamma_\mu D_{(\Delta)}^\mu - m_\Delta^*) \psi_\Delta^\nu + \frac{1}{2} (\partial_\mu \sigma \partial^\mu \sigma - m_\sigma^2 \sigma^2) \\ & - \frac{1}{4} \omega_{\mu\nu} \omega^{\mu\nu} + \frac{1}{2} m_\omega^2 \omega_\mu \omega^\mu - \frac{1}{4} \rho_{\mu\nu} \cdot \rho^{\mu\nu} + \frac{1}{2} m_\rho^2 \rho_\mu \cdot \rho^\mu \\ & - \frac{1}{4} \phi_{\mu\nu} \phi^{\mu\nu} + \frac{1}{2} m_\phi^2 \phi_\mu \phi^\mu - U(\sigma) \end{aligned} \quad (1)$$

where, the last term $U(\sigma)$ corresponds to the self-interactions of scalar mesons only for NLW CDF models. ψ_b , ψ_l , ψ_Δ^ν represent Dirac-fields of the baryon-octet, leptons and Schwinger-Rarita fields of Δ -quartet respectively. m_b , m_l , m_Δ denote the bare masses of baryon octet, leptons and Δ -quartet species respectively. The covariant derivative mentioned in eq.(1) is given by

$$D_{\mu(j)} = \partial_\mu + ig_{\omega j} \omega_\mu + ig_{\rho j} \tau_{j3} \cdot \rho_\mu + ig_{\phi j} \phi_\mu \quad (2)$$

with j denoting the baryon octet (b) and Δ -quartet (Δ). The coupling constants are represented by g_{pj} with index- p being the considered mesons. τ_{j3} is the iso-spin projection of third component of isovector-vector meson fields. The scalar self-interaction term for NLW CDF model is given by

$$U(\sigma) = \frac{1}{3} g_2 \sigma^3 + \frac{1}{4} g_3 \sigma^4 \quad (3)$$

where g_2 and g_3 are the coefficients of self-interactions.

With the monotonic increase in baryon chemical potentials inferior to NSs, the nucleonic matter may well transform to heavier strange and non-strange baryons leading to new hadronic degrees of freedom. The conditions which are necessary to maintain strong β -equilibrium between different particle species without strangeness being conserved are (Banik & Bandyopadhyay 2001; Drago et al. 2014)

$$\begin{aligned} \mu_e = \mu_n - \mu_p = \mu_\mu, \quad \mu_{\Sigma^+} = \mu_{\Delta^+} = \mu_p, \\ \mu_{\Sigma^-} = \mu_{\Xi^-} = \mu_{\Delta^-} = \mu_n + \mu_e, \quad \mu_{\Delta^{++}} = \mu_p - \mu_e, \\ \mu_{\Sigma^0} = \mu_{\Xi^0} = \mu_{\Lambda^0} = \mu_{\Delta^0} = \mu_n \end{aligned} \quad (4)$$

with μ_j denoting chemical potential of the j -th baryon and defined as

$$\mu_j = \sqrt{p_{F_j}^2 + m_j^{*2}} + \Sigma_B. \quad (5)$$

Here, $\Sigma_B = \Sigma^0 + \Sigma^r$ represents the vector self energies with $\Sigma^0 = g_{\omega j} \omega_0 + g_{\phi j} \phi_0 + g_{\rho j} \tau_{j3} \rho_{03}$ and Σ^r denotes the re-arrangement term (present in DD CDF models only) necessary to maintain thermodynamic consistency which is given by

$$\begin{aligned} \Sigma^r = & \sum_b \left[\frac{\partial g_{\omega b}}{\partial n} \omega_0 n_b - \frac{\partial g_{\sigma b}}{\partial n} \sigma n_b^s + \frac{\partial g_{\rho b}}{\partial n} \rho_{03} \tau_{b3} n_b \right. \\ & \left. + \frac{\partial g_{\phi b}}{\partial n} \phi_0 n_b \right] + \sum_\Delta (\psi_b \rightarrow \psi_\Delta^r), \end{aligned} \quad (6)$$

with $n^s = \langle \bar{\psi} \psi \rangle$ and $n = \langle \bar{\psi} \gamma^0 \psi \rangle$ denoting the scalar and vector (number) densities respectively.

Two additional constraints, viz. charge neutrality and global baryon number conservation, are administered while evaluating the EOS self-consistently. The re-arrangement term considered in DD CDF model contributes explicitly to the pressure term. For details, the readers may refer to Hofmann et al. (2001).

3.2 Tidal deformability

The compact stars in a binary system experience tidal deformations due to the gravitational fields of their respective companions. These tidal effects can be quantified in terms of tidal deformability parameter (λ) defined as the ratio of induced mass quadrupole moment Q_{ij} to external perturbing tidal field \mathcal{E}_{ij} (Hinderer 2008; Flanagan & Hinderer 2008; Hinderer et al. 2010),

$$\lambda = -\frac{Q_{ij}}{\mathcal{E}_{ij}} = \frac{2}{3} k_2 R^5, \quad (7)$$

where,

$$\begin{aligned} k_2 = & \frac{8C^5}{5} (1 - 2C^2) [2 + 2C(y - 1) - y] \cdot \{2C[6 - 3y + 3C(5y - 8)] \\ & + 4C^3[13 - 11y + C(3y - 2) + 2C^2(1 + y)] + 3(1 - 2C^2) \cdot \\ & [2 - y + 2C(y - 1)] \log(1 - 2C)\}^{-1} \end{aligned} \quad (8)$$

with $C = M/R$ being the compactness parameter, M and R being mass and radius of the star respectively and k_2 , the EOS dependent tidal Love number. $y = y(R)$ is the function obtained after solving the differential equation (Binnington & Poisson 2009; Damour & Nagar 2010; Kumar et al. 2017),

$$r \frac{dy(r)}{dr} + y(r)^2 + y(r)F(r) + r^2 Q(r) = 0, \quad (9)$$

where the functions are

$$F(r) = \frac{r - 4\pi r^3 [\varepsilon(r) - P(r)]}{r - 2M(r)}, \quad (10)$$

$$Q(r) = \frac{4\pi r [5\varepsilon(r) + 9P(r) + \frac{\varepsilon(r)+P(r)}{\partial P(r)/\partial \varepsilon(r)}]}{r - 2M(r)} - 4 \left[\frac{M(r) + 4\pi r^3 P(r)}{r^2(1 - 2M(r)/r)} \right]. \quad (11)$$

Due to paramount dependence on the stellar radius, λ imposes stringent constraints on dense matter EOS. λ or, equivalently k_2 provides the ease of induced deformation estimate of bulk matter.

Table 1. The nuclear properties of the CDF models at respective n_0 .

| CDF Model | n_0 (fm^{-3}) | $-E_0$ (MeV) | K_0 (MeV) | E_{sym} (MeV) | L_{sym} (MeV) | K_{sym} (MeV) | |
|-----------|-------------------------------|-----------------|----------------|---------------------------|---------------------------|---------------------------|---------|
| GM1 | 0.153 | 16.30 | 300.00 | 32.50 | 93.857 | 17.91 | |
| GM2 | 0.153 | 16.30 | 300.00 | 32.50 | 89.289 | -11.98 | |
| GM3 | 0.153 | 16.30 | 240.00 | 32.50 | 89.627 | -6.46 | |
| NLW | NL3 | 0.148 | 16.29 | 271.76 | 37.40 | 118.317 | 100.53 |
| | NL3-II | 0.149 | 16.28 | 272.15 | 37.70 | 119.563 | 103.19 |
| | NL-SH | 0.146 | 16.346 | 355.36 | 36.10 | 113.654 | 79.81 |
| | NL-RA1 | 0.1466 | 16.15 | 285.00 | 36.10 | 115.305 | 95.57 |
| | NL3* | 0.150 | 16.31 | 258.27 | 38.68 | 122.71 | 105.73 |
| | GMT | 0.145 | 16.30 | 281.00 | 36.90 | 112.796 | 63.04 |
| DD | DD1 | 0.1487 | 16.021 | 240.00 | 31.60 | 55.949 | -95.24 |
| | DD2 | 0.149065 | 16.02 | 242.70 | 32.73 | 54.966 | -93.24 |
| | DD-ME1 | 0.152 | 16.20 | 244.50 | 33.10 | 55.370 | -101.07 |
| | DD-ME2 | 0.152 | 16.14 | 250.89 | 32.30 | 51.253 | -87.31 |
| | PKDD | 0.149552 | 16.267 | 262.181 | 36.79 | 90.139 | -80.56 |
| | TW99 | 0.153 | 16.247 | 240.00 | 33.39 | 55.309 | -124.68 |
| | DDV | 0.151 | 16.097 | 240.00 | 33.589 | 71.463 | -93.97 |
| | DDF | 0.1469 | 16.024 | 223.10 | 31.60 | 55.919 | -139.66 |
| | DD-MEX | 0.152 | 16.14 | 267.059 | 32.269 | 49.576 | -71.47 |

This parameter is evaluated self-consistently alongside the Tolman-Oppenheimer-Volkov (TOV) equations (Glendenning 1996). Another dimensionless quantity Λ is much more expedient as it relates λ with C through the relation

$$\Lambda = \frac{\lambda}{M^5} = \frac{2}{3} \frac{k_2}{C^5}. \quad (12)$$

GW signal encodes information regarding deformation of both compact objects in the binary system as the weighted tidal deformability ($\tilde{\lambda}$) and is given by (Hinderer 2008; Hinderer et al. 2010)

$$\tilde{\lambda} = \frac{1}{26} \left[\frac{M_1 + 12M_2}{M_1} \lambda_1 + \frac{M_2 + 12M_1}{M_2} \lambda_2 \right] \quad (13)$$

where λ_1 , λ_2 are the tidal deformabilities corresponding to stars with masses M_1 , M_2 respectively. In order to relate to Λ , we incorporate the combined dimensionless tidal deformability ($\tilde{\Lambda}$) defined as (Favata 2014)

$$\tilde{\Lambda} = 32 \frac{\tilde{\lambda}}{(M_1 + M_2)^5} = \frac{16}{13} \frac{(M_1 + 12M_2)M_1^4 \Lambda_1 + (M_2 + 12M_1)M_2^4 \Lambda_2}{(M_1 + M_2)^5}. \quad (14)$$

3.3 Coupling parameters

In this work, we adopt the NLW model with GM1, GM2, GM3 (Glendenning & Moszkowski 1991b), NL3, NL3-II (Lalazissis et al. 1997), NL-SH (Sharma et al. 1993), NL-RA1 (Rashdan 2001), NL3* (Lalazissis et al. 2009), GMT (Pal et al. 2000) parameterizations and the DD CDF model with DD1 (Typel 2005), DD2 (Typel et al. 2010), DD-ME1 (Nikšić et al. 2002), DD-ME2 (Lalazissis et al. 2005), PKDD (Long et al. 2004), TW99 (Typel & Wolter 1999), DDV (Typel & Alvear Terrero 2020), DDF (Klähn et al. 2006), DD-MEX (Taninah et al. 2020) parameterizations for meson-baryon couplings.

Comparison of experimental data (Oertel et al. 2017) from finite nuclei and heavy-ion collisions with different microscopic model calculations have provided bounds on nuclear saturation properties of symmetric nuclear matter (SNM):

- (i) Incompressibility, $210 \leq K_0(n_0) \leq 280$ MeV,
- (ii) Symmetry energy coefficient, $28.5 \leq E_{\text{sym}}(n_0) \leq 34.9$ MeV,

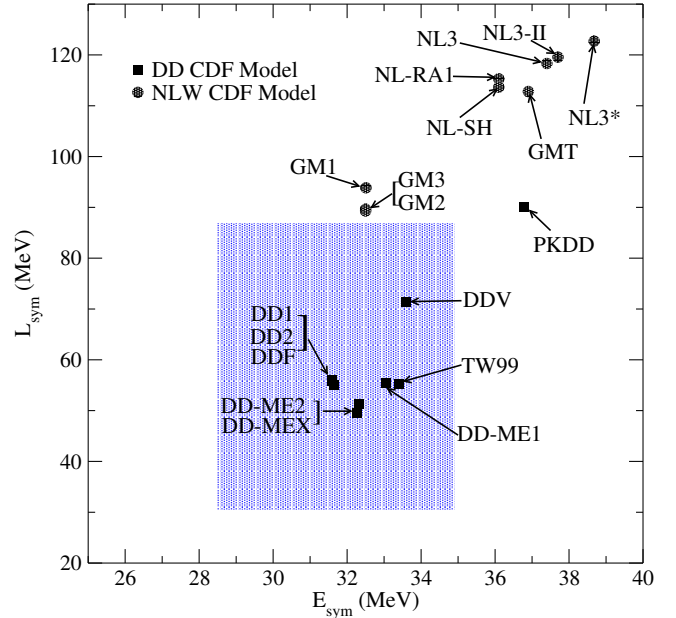


Figure 1. Symmetry energy coefficient (E_{sym}) and its corresponding slope parameter (L_{sym}) for all the parametrization models considered in this work. The shaded region represents the current empirical range in $E_{\text{sym}}-L_{\text{sym}}$ plane following recent experimental and microscopic model calculations (Oertel et al. 2017).

- (iii) Slope parameter of E_{sym} , $30.6 \leq L_{\text{sym}}(n_0) \leq 86.8$ MeV.

Table-1 displays the nuclear saturation properties obtained for models with different CDF parameterizations considered in this work with E_0 , the saturation energy. The bounds on curvature of symmetry energy, $K_{\text{sym}}(n_0) = -111.8 \pm 71.3$ MeV (Mondal et al. 2017), -85^{+82}_{-70} MeV (Baillot d'Étivaux et al. 2019), -102^{+71}_{-72} MeV (Zimmerman et al. 2020) deduced from nuclear data and various NS observations provide additional constraint on dense matter EOS.

The density-dependent meson-nucleon couplings implemented in DD CDF model are defined as (Typel & Wolter 1999; Nikšić et al.

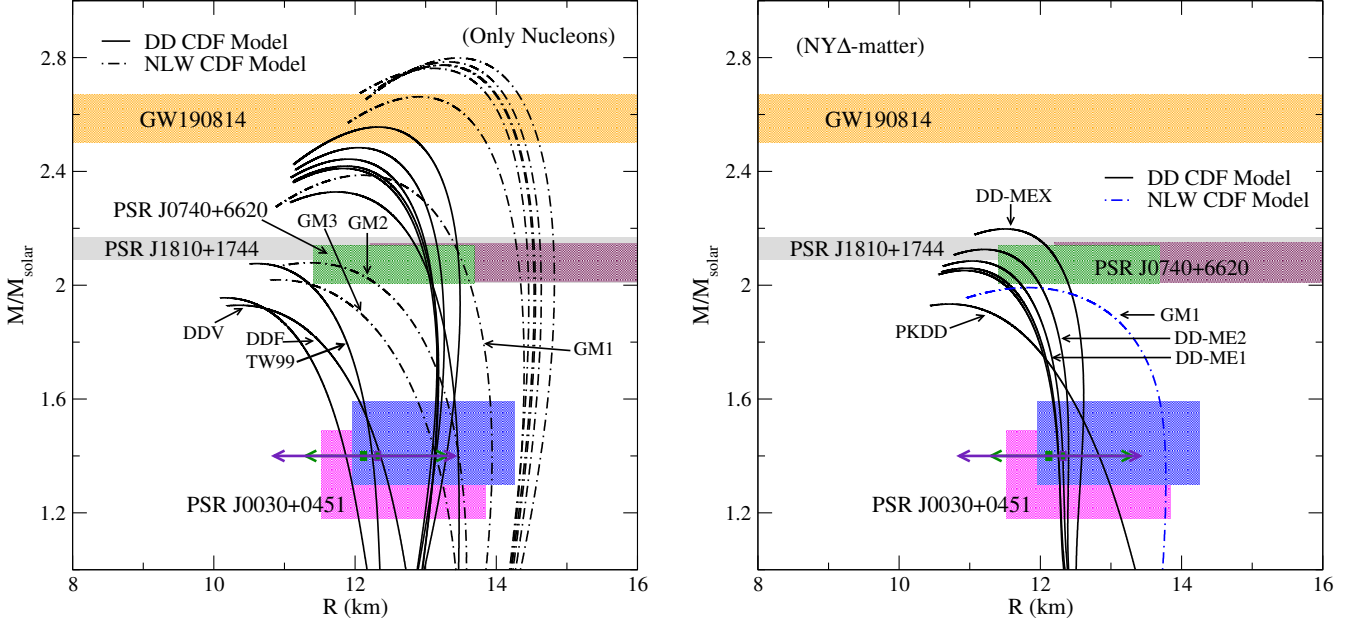


Figure 2. The family of solutions of TOV equations for matter composed of, left panel: only nucleons and right panel: Δ -admixed hypernuclear matter alongside leptons to maintain β -equilibrium. The solid curves denote the M - R curves for different density-dependent model parametrizations, while the dot-dashed curves denote the cases with non-linear model parametrizations. The astrophysical constraints from GW190814 (Abbott et al. 2020b), PSR J1810+1744 (Romani et al. 2021), PSR J0030+0451 (Miller et al. 2019; Riley et al. 2019; Jiang et al. 2020; Landry et al. 2020), PSR J0740+6620 (Riley et al. 2021; Miller et al. 2021) are represented by the shaded regions.

2002),

$$g_{iN}(n) = g_{iN}(n_0) f_i(n/n_0) \quad \text{for } i = \sigma, \omega \quad (15)$$

where, n is the baryon number density and

$$f_i(n/n_0) = a_i \frac{1 + b_i(n/n_0 + d_i)^2}{1 + c_i(n/n_0 + d_i)^2}. \quad (16)$$

In the case of ρ -meson couplings, the functional is defined as

$$g_{\rho N}(n) = g_{\rho N}(n_0) e^{-a_\rho(n/n_0-1)}. \quad (17)$$

For the coefficient values in Eqs.(15)-(17), the readers may refer to Typel (2005); Typel et al. (2010); Nikšić et al. (2002); Lalazissis et al. (2005); Long et al. (2004); Typel & Wolter (1999); Typel & Alvar Terrero (2020); Klähn et al. (2006); Taninah et al. (2020). These coefficients are associated with different DD CDF model parametrizations and fitted to reproduce various nuclei properties. The hidden strangeness meson ϕ doesn't couple with nucleons, so $g_{\phi N} = 0$.

The meson-hyperon and meson- Δ couplings are considered similar to the density-dependence footing in the case of nucleons in DD CDF model. In the case of the meson-hyperon vector couplings, we implement the SU(6) symmetry and quark counting rule (Schaffner et al. 1994). For the scalar meson-hyperon couplings, we consider the optical potentials of Λ , Σ , Ξ -hyperons in SNM to be $-28, +30, -14$ MeV respectively at nuclear saturation (Felicciello & Nagee 2015; Gal et al. 2016). The optical potential depths $U_{\Xi}^{(N)}(n_0) = -18$ MeV, $U_{\Lambda}^{(N)}(n_0) = -30$ MeV (Schaffner-Bielich & Gal 2000; Gomes et al. 2015) are also widely implemented in dense matter studies. Recently ref.-(Friedman & Gal 2021) reported an attractive optical potential depth of Ξ -hyperons in SNM to be $\gtrsim -20$ MeV. For a more recent review on the aspects of strangeness in dense matter, the reader may refer to Ref.-Tolos & Fabbietti (2020).

Due to scarce information regarding the Δ -nucleon interactions, we treat the meson- Δ resonances couplings as parameters. Nakamura et al. (2010); Koch & Ohtsuka (1985); Wehrberger et al. (1989) have reported the data to constrain meson- Δ baryon couplings at n_0 based on pion-nucleus scattering, electron scattering on nuclei and excitation studies of Δ -quartet experiments. Recent reviews (Drago et al. 2014; Klähn et al. 2006; Kolomeitsev et al. 2017) on this aspect have reported the Δ -potential (V_{Δ}) in nuclear medium to be in the range $-30 \text{ MeV} + V_N \leq V_{\Delta} \leq V_N$ (V_N being the nucleon potential), the values of factor $x_{\sigma\Delta} - x_{\omega\Delta}$ to be between 0 and 0.2 with $x_{\sigma\Delta} = g_{\sigma\Delta}/g_{\sigma N}$ and $x_{\omega\Delta} = g_{\omega\Delta}/g_{\omega N}$. Many works (Drago et al. 2014; Kolomeitsev et al. 2017; Li et al. 2018c; Ribes et al. 2019; Chen et al. 2007; Cai et al. 2015; Raduta 2021) have considered the ranges for $x_{\omega\Delta} \in [0.6 - 1.2]$ and $x_{\rho\Delta} \in [0.5 - 3.0]$. For recent development regarding Δ -potential in dense matter, the reader may refer to Ref.-Cozma & Tsang (2021). In the ensuing discussion, we will consider $x_{\omega\Delta} = 1.10$, $x_{\rho\Delta} = 1.00$ for the vector meson- Δ baryon couplings and $x_{\sigma\Delta} = 1.20$ for the scalar coupling. Δ -quartet being non-strange baryons does not couple with ϕ -meson, so $g_{\phi\Delta} = 0$.

4 CONSTRAINTS ON DENSE MATTER MODELS

Next, we sort out the different EOSs with various possible compositions and parametrizations based on terrestrial experimental and stellar observational values. From table-1 it can be noticed that all the models reproduce n_0 and E_0 in the correct range of empirical values. However, among the NLW parametrizations considered in this work, GM1 and GM2 cannot reproduce the empirical range of K_0 at n_0 mentioned in Sec.-3.3, while all the DD CDF models considered in this work satisfy the empirical range of K_0 at n_0 . On the other hand, the empirical range of symmetry energy coefficient is satisfied by GM1, GM2, GM3 parameter sets among NLW models, while in

Table 2. Summary of TOV results evaluated from parameter sets considered in this work (pure N -matter, refer to left panel of fig.-2). Fulfillment of the mass-radius constraints from various astrophysical observations are marked by +(-).

| CDF Model | PSR J0030 + 0451 | PSR J0740 + 6620 | PSR J1810 + 1744 | GW190814 (secondary)** |
|-----------|------------------|------------------|------------------|------------------------|
| GM1 | + | + | + | - |
| GM2 | + | + | - | - |
| GM3 | + | - | - | - |
| NL3 | - | + | + | + |
| NL3-II | - | + | + | + |
| NL-SH | - | + | + | + |
| NL-RA1 | - | + | + | + |
| NL3* | - | + | + | + |
| GMT | - | + | + | + |
| DD1 | + | + | + | - |
| DD2 | + | + | + | - |
| DD-ME1 | + | + | + | - |
| DD-ME2 | + | + | + | - |
| PKDD | + | + | + | - |
| TW99 | + | - | - | - |
| DDV | + | - | - | - |
| DDF | + | - | - | - |
| DD-MEX | + | + | + | + |

** The nature of secondary component of GW190814 is still in tension

the case of DD models, all except PKDD parametrization lie within the bounds of this particular saturation property. The current empirical bound on L_{sym} is satisfied by all DD parametrization models considered in this work except PKDD parametrization. In addition, the current empirical bounds on K_{sym} are satisfied by GM2, GM3 (among NLW models) and all DD parameter sets considered in this work. Fig.-1 displays the parameter sets which are compatible with the current bounds on E_{sym} and L_{sym} . All the DD models (except PKDD) considered in this work satisfy the current bounds on nuclear saturation properties.

The mass-radius (M - R) relations corresponding to the various parameterizations for only nucleonic matter composition, are shown in left panel of fig.-2 obtained by solving the TOV equations for spherically symmetric, non-rotating stars. For the crustal region, we consider the Baym et al. (1971) EOS. The transition from crust to the core is modelled in a way that is thermodynamically consistent following Ref.-Fortin et al. (2016). We consider the recent massive NS observation (PSR J1810+1744) as the lower bound for maximum mass configurations. If we consider pure nucleonic matter, all the EOSs considered in this work except a few satisfy the lower bound constraint of maximum mass as evident from left panel of fig.-2. GM2 ($M_{\text{max}} \sim 2.08 M_{\odot}$), GM3 ($2.02 M_{\odot}$) among NLW type and TW99 ($2.07 M_{\odot}$), DDV ($1.93 M_{\odot}$), DDF ($1.96 M_{\odot}$) among DD type models fail to satisfy this mass constraint. However, the constraints obtained from NICER observations (PSR J0030 + 0451) are seen to be not satisfied by the NLW models satisfying mass constraint, except the GM1 parametrization, while all the DD type models satisfying the mass constraint satisfy this constraint too. Moreover, these models satisfy the recent NICER results of PSR J0740+6620 simultaneously. Here, PSR J0740 + 6620 observation suggests the dense matter at higher densities is repulsive enough to produce large radii of heavier NSs. Most of the NLW models not satisfying the NICER observations

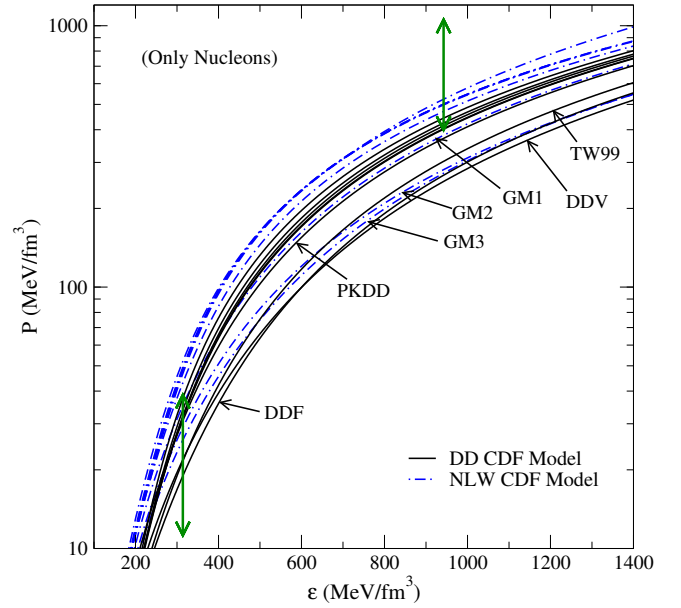


Figure 3. The variation of matter pressure as a function of energy density (EOS) for β -equilibrated matter composed of only nucleons and leptons. The solid curves denote the EOSs for different density-dependent model parametrizations, while the dot-dashed curves denote the cases with non-linear model parametrizations. The constraints on matter pressure evaluated from GW170817 event are denoted by the vertical lines and provided in sec.-1.

of PSR J0030 + 0451 are observed to satisfy this recent constraint with a wider radii range. However, even though they are observed to fulfil the constraint from Miller et al. (2021), they fail to fulfil another NICER measurement of PSR J0030+0451 from Miller et al. (2019); Riley et al. (2019); Jiang et al. (2020); Landry et al. (2020). Stiffer EOSs (N -matter) obtained from NLW type parametrizations (except GM1, GM2, GM3) and DD-MEX (DD type) yield $M_{\text{max}} \geq 2.5 M_{\odot}$ satisfying the GW190814 event secondary component's mass constraint. Although this constraint is not unequivocal as the nature of secondary compact object is not found to be NS explicitly (Sedrakian et al. 2020; Li et al. 2020b). The TOV results involving different parametrizations with pure N -matter are summarized in table-2. As a result of EOS softening due to the inclusion of hyperons and Δ -quartet, the only NLW model EOS with the GM1 parametrization, satisfying all mass-radius constraints, produce stars that fail to fulfil the lower bound constraint of maximum mass as shown in right panel of fig.-2. Except PKDD ($M_{\text{max}} \sim 1.93 M_{\odot}$), DD1 ($2.05 M_{\odot}$), DD2 ($2.06 M_{\odot}$) parametrizations all other parametrizations from DD CDF models which satisfy the joint constraints from PSR J1810 + 1744, PSR J0740 + 6620 and PSR J0030 + 0451 with pure N -matter satisfy the mass constraints even after softening due to hyperonization. The incorporation of Δ -quartet reduces the radii of NSs, enhancing their respective compactness parameter.

We now look into the pressure bounds in lower and higher matter density regimes derived from GW170817 event data. Fig.-3 shows that all the EOSs with pure nuclear matter satisfying mass-radius constraints also satisfy both the pressure bounds. It is to be noted that among NLW models, GM1, GM2 and GM3 satisfy only the lower bound at $n \sim 2n_0$ while they fail to satisfy the bound at $n \sim 6n_0$. It has to be kept in mind that the estimated bound at $6n_0$ is more than the central pressures of compact stars involved in GW170817 event.

We have evaluated $\tilde{\Lambda}$ with the range of primary and secondary masses $1.36 - 1.60 M_{\odot}$ and $1.17 - 1.36 M_{\odot}$ respectively to provide

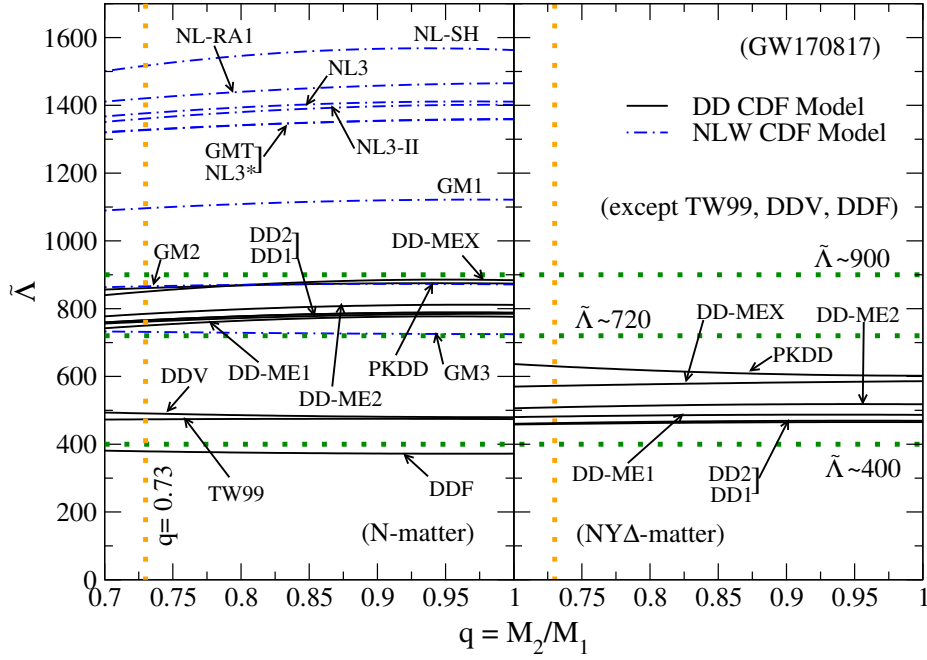


Figure 4. Combined dimensionless tidal deformability as a function of mass-ratio (q) considering a fixed chirp mass, $\mathcal{M} = 1.188 M_{\odot}$ (GW170817 event). Left panel: nucleonic matter, right panel: Δ -resonances and baryon octet matter. The solid, dot-dashed lines depicts the DD and NLW type parametrizations respectively. The parametrizations yielding soft EOSs are not shown in the right panel. The horizontal dotted lines denote bounds on $\tilde{\Lambda}$ (with 90% credibility, low-spin priors). The vertical dotted lines represent the mass-ratio, $q = 0.73$ boundary (Abbott et al. 2019).

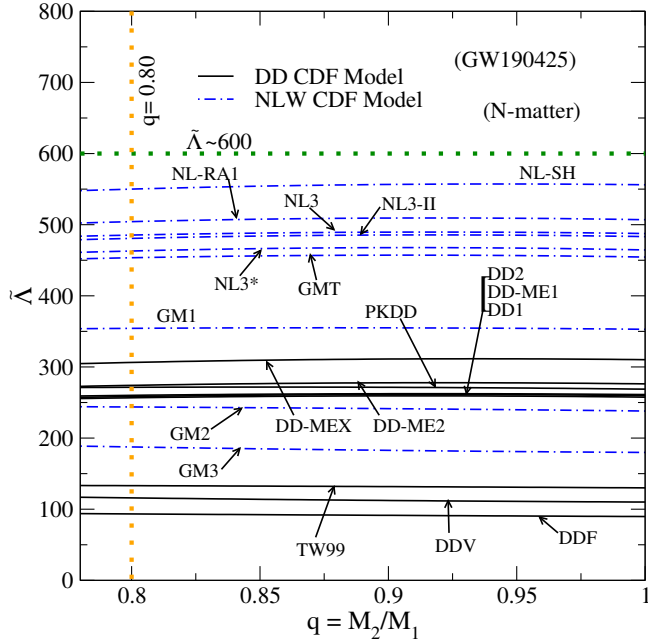


Figure 5. Similar to fig.-4 but considering a fixed chirp mass, $\mathcal{M} = 1.43 M_{\odot}$ (GW190425 event) with pure nucleonic matter. The solid, dot-dashed lines depicts the DD and NLW type parametrizations respectively. $\tilde{\Lambda}$ constraints are similar to fig.-4. The vertical dotted lines represent the mass-ratio, $q = 0.80$ boundary (Abbott et al. 2020a).

the chirp mass, $\mathcal{M} = (M_1 M_2)^{3/5} (M_T)^{-1/5} = 1.188 M_{\odot}$ where the total mass $M_T = M_1 + M_2$, is in the range $2.73 - 2.78 M_{\odot}$ for GW170817 event. In this work, we have considered the source

properties to be circumscribing within 90% credible intervals. Fig.-4 shows the $\tilde{\Lambda}$ variation with mass-ratio parameter (q). $\tilde{\Lambda}$ is found to be almost independent of the mass asymmetry factor q (refer to table-3 for numerical results). In the left panel, curves are for pure nucleonic matter and in the right panel, they are for Δ -admixed hypernuclear matter. For pure nucleonic matter, only GM2, GM3 models lie within the observational $\tilde{\Lambda} \sim 900$ bound among the NLW CDF models. However, they do not satisfy the lower bound constraint of maximum mass. In DD CDF models, all parametrizations considered in this work follow the upper bound of 900. The stringent limit of $\tilde{\Lambda} \sim 720$ is observed to be satisfied by only TW99, DDV, DDF models which do not satisfy lower bound constraint for maximum mass. With Δ -baryons coming into the picture, the models fulfil the latter stringent upper bound on $\tilde{\Lambda}$ as shown from the right panel of the figure. Since the effect of hyperon inclusion on $\tilde{\Lambda}$ is similar to that of nucleons for the NSs with mass bounds obtained from GW170817 event, so they are not shown in fig.-4.

Similar to fig.-4, the effective tidal deformability as a function of mass-asymmetry factor q corresponding to the GW190425 event with a fixed chirp mass, $\mathcal{M} = 1.43 M_{\odot}$ for all the parametrizations considered in this work is shown in fig.-5 with only nucleonic matter. In this case, masses of the two compact stars are varied in the ranges $1.60 \leq M_1/M_{\odot} \leq 1.87$ (primary) and $1.46 \leq M_2/M_{\odot} \leq 1.69$ (secondary) (Abbott et al. 2020a). Weak dependence of $\tilde{\Lambda}$ on q can be inferred. It is observed that all the parametrizations satisfy the upper bound constraint on $\tilde{\Lambda}$ provided by GW190425 event data. Consequently this GW event does not provide enough information to put strict limits on constraining dense matter EOSs. Inclusion of Δ -quartet will decrease $\tilde{\Lambda}$ compared to pure nucleonic case.

We next evaluate the tidal deformabilities (Λ_1, Λ_2) of binary components involved in GW170817 event with different matter compositions. For the evaluation of Λ_1 and Λ_2 , we consider $\mathcal{M} = 1.188 M_{\odot}$

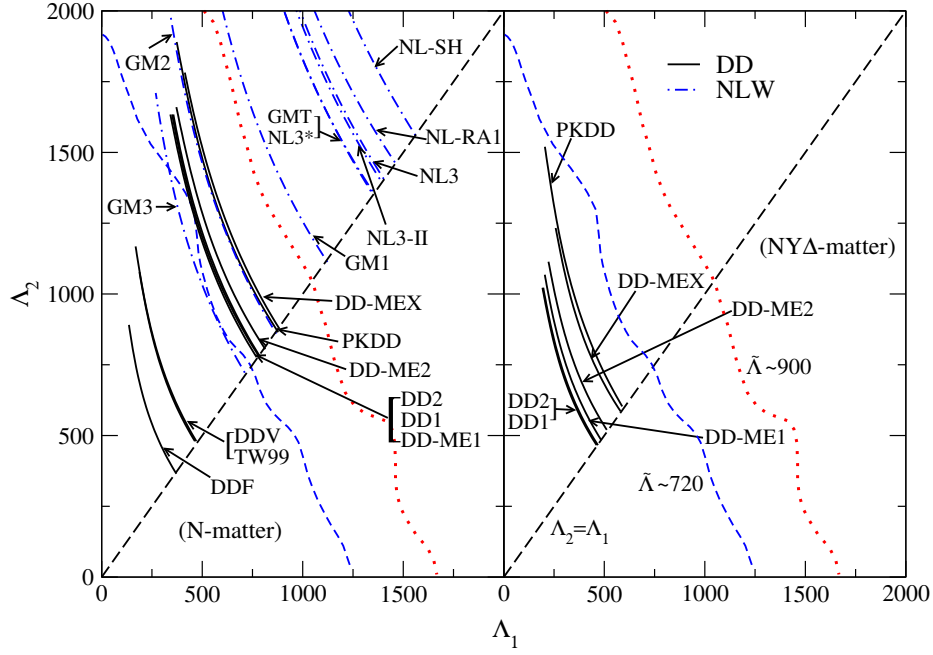


Figure 6. Tidal deformability parameters Λ_1, Λ_2 corresponding to the binary components, M_1, M_2 for GW170817 event with matter composition as, left panel: pure nucleonic matter, right panel: Δ -baryon admixed hypernuclear and assuming a fixed chirp mass, $\mathcal{M} = 1.188 M_\odot$. The solid curves denote the DD type parametrizations while the NLW type are denoted by dash-dotted curves. The dotted, short-dashed curves denote the $\tilde{\Lambda} \sim 900$ (TaylorF2), 720 (PhenomPNRT) upper bounds at 90% confidence level (low-spin priors) respectively (Abbott et al. 2017a, 2019). The diagonal long-dashed line marks $\Lambda_1 = \Lambda_2$ case.

Table 3. Observational properties of various CDF models with different matter compositions. Here, q represents the mass ratio of the secondary component (M_2) to primary one (M_1) involved in GW event. $C_{1,4}$ denotes the compactness parameter for a $1.4M_\odot$ NS.

| Matter composition | CDF Model | M_{\max} (M_\odot) | $R_{1,4}$ (km) | $\Lambda_{1,4}$ | $C_{1,4}$ | $\tilde{\Lambda} (q = 0.8)$ | | $\tilde{\Lambda} (q = 1.0)$ | |
|---------------------------------------|---------------------|--------------------------|----------------|-----------------|-----------|-----------------------------|----------|-----------------------------|----------|
| | | | | | | GW170817 | GW190425 | GW170817 | GW190425 |
| Pure Nucleonic Matter | GM1 | 2.387 | 13.939 | 966.34 | 0.148 | 1109.39 | 355.77 | 1121.63 | 358.93 |
| | GM2 | 2.079 | 13.468 | 743.19 | 0.153 | 870.59 | 246.12 | 871.51 | 244.33 |
| | GM3 | 2.019 | 13.146 | 607.88 | 0.157 | 724.64 | 189.05 | 728.79 | 184.81 |
| | NL3 | 2.774 | 14.430 | 1222.72 | 0.143 | 1394.86 | 489.88 | 1410.87 | 495.58 |
| | NL3-II | 2.773 | 14.408 | 1217.59 | 0.143 | 1381.14 | 483.69 | 1401.64 | 494.33 |
| | NL-SH | 2.799 | 14.630 | 1368.94 | 0.141 | 1547.36 | 554.41 | 1563.07 | 565.93 |
| | NL-RA1 | 2.785 | 14.490 | 1278.05 | 0.143 | 1440.78 | 508.58 | 1465.28 | 518.21 |
| | NL3* | 2.762 | 14.355 | 1181.41 | 0.144 | 1341.70 | 465.63 | 1358.48 | 476.51 |
| | GMT | 2.662 | 14.355 | 1177.91 | 0.144 | 1342.24 | 456.92 | 1359.93 | 462.36 |
| | DD1 | 2.410 | 13.126 | 678.92 | 0.157 | 772.75 | 259.42 | 784.91 | 261.88 |
| | DD2 | 2.418 | 13.133 | 683.97 | 0.157 | 778.13 | 261.79 | 787.99 | 265.77 |
| | DD-ME1 | 2.443 | 13.086 | 672.37 | 0.158 | 765.14 | 261.09 | 776.04 | 266.31 |
| | DD-ME2 | 2.483 | 13.146 | 706.08 | 0.157 | 798.93 | 276.48 | 811.16 | 281.47 |
| | PKDD | 2.328 | 13.461 | 750.66 | 0.154 | 869.05 | 273.56 | 874.03 | 275.28 |
| | Hypernuclear Matter | TW99 | 2.076 | 12.245 | 402.46 | 0.169 | 474.17 | 134.40 | 474.57 |
| DDV | | 1.929 | 12.360 | 398.67 | 0.167 | 485.52 | 117.40 | 479.76 | 112.95 |
| DDF | | 1.956 | 11.871 | 311.618 | 0.174 | 372.22 | 94.59 | 375.27 | 91.84 |
| DD-MEX | | 2.556 | 13.293 | 773.49 | 0.156 | 869.28 | 309.58 | 883.91 | 316.32 |
| DD1 | | 2.039 | 13.124 | 680.44 | 0.158 | 777.19 | 262.33 | 783.48 | 264.47 |
| DD2 | | 2.046 | 13.132 | 684.61 | 0.157 | 784.18 | 265.08 | 793.09 | 267.20 |
| DD-ME1 | | 2.075 | 13.086 | 673.16 | 0.158 | 773.05 | 265.19 | 778.05 | 267.71 |
| DD-ME2 | | 2.115 | 13.146 | 707.53 | 0.157 | 808.16 | 277.39 | 813.83 | 282.33 |
| PKDD | | 1.943 | 13.444 | 744.97 | 0.154 | 866.23 | 269.07 | 870.23 | 273.08 |
| DD-MEX | | 2.186 | 13.293 | 773.49 | 0.156 | 873.62 | 312.38 | 884.72 | 319.36 |
| Δ -admixed Hypernuclear Matter | DD1 | 2.052 | 12.254 | 398.11 | 0.169 | 462.63 | 137.06 | 465.33 | 138.56 |
| | DD2 | 2.059 | 12.260 | 402.03 | 0.169 | 466.22 | 139.86 | 469.16 | 140.69 |
| | DD-ME1 | 2.085 | 12.320 | 418.19 | 0.168 | 485.03 | 146.52 | 486.65 | 148.15 |
| | DD-ME2 | 2.126 | 12.400 | 444.20 | 0.167 | 514.21 | 160.55 | 517.89 | 163.58 |
| | PKDD | 1.934 | 12.832 | 501.68 | 0.161 | 617.18 | 144.53 | 602.05 | 136.74 |
| | DD-MEX | 2.198 | 12.588 | 503.30 | 0.164 | 577.19 | 189.24 | 586.07 | 192.52 |

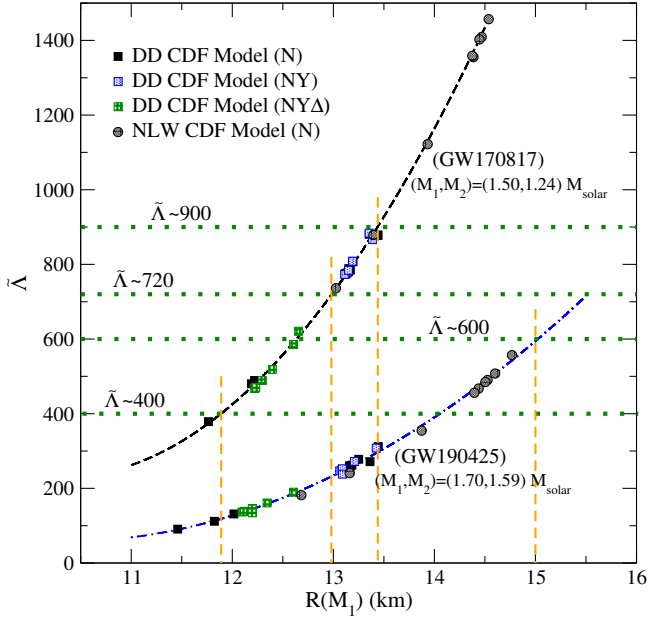


Figure 7. Effective tidal deformability variation with radius of the binary’s primary component for GW170817 and GW190425 events. The solid, dotted, striped squares represent the DD parametrizations with pure nucleonic, baryon octet, Δ -admixed hypernuclear matter respectively. The solid circles denote the NLW parametrizations with nucleonic matter case. The quadratic correlations for the GW170817, GW190425 cases are given by short-dashed and dash-dotted curves respectively. The horizontal dotted lines represent bounds on $\tilde{\Lambda}$ similar to figs.-4,5. The vertical short-dashed lines mark the points where the quadratic fits intersect $\tilde{\Lambda}$ bounds.

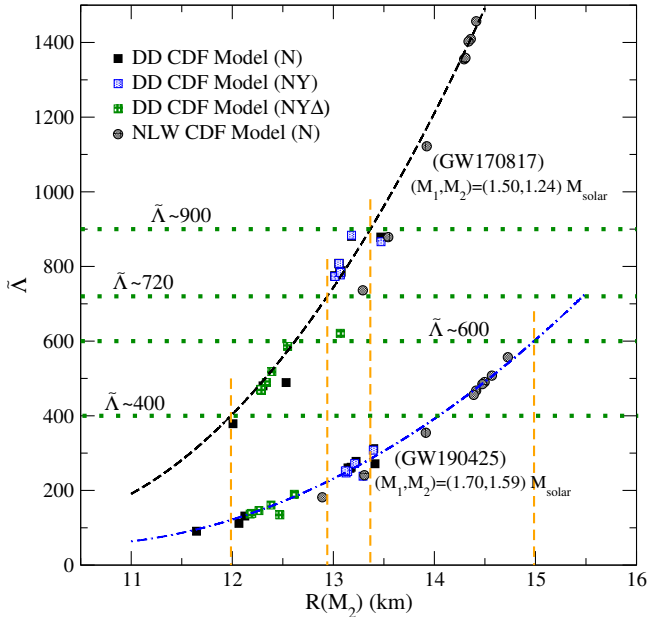


Figure 8. Similar to fig.-7 but for secondary components of GW170817 and GW190425 events. The solid, dotted, striped squares represent the DD parametrizations with pure nucleonic, baryon octet, Δ -admixed hypernuclear matter respectively. The solid circles denote the NLW parametrizations with nucleonic matter case. The quadratic correlations for the GW170817, GW190425 cases are given by short-dashed and dash-dotted curves respectively. $\tilde{\Lambda}$ constraints are similar to fig.-7.

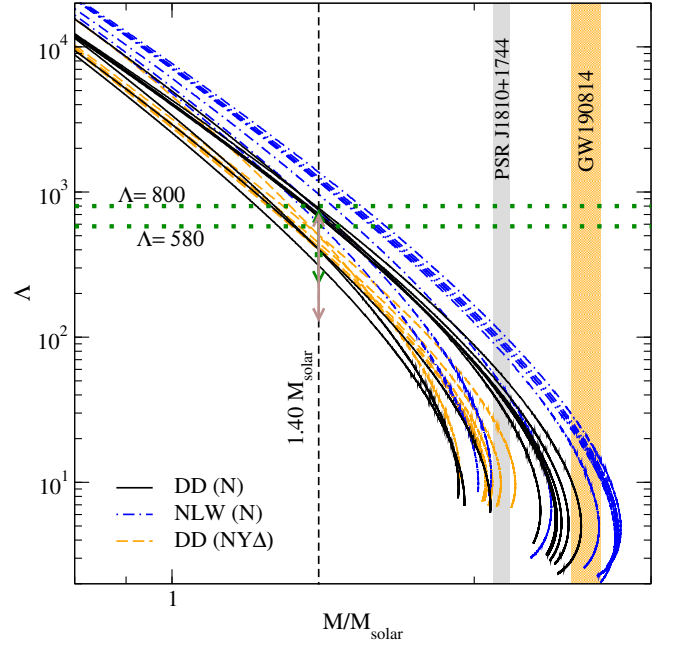


Figure 9. Dimensionless tidal deformability (Λ) as a function of the NS mass (M) for CDF model parametrizations considered in this work (with N , $NY\Delta$ -matter). DD, NLW type models with N -matter are represented similar to fig.-2,3. While DD models with $NY\Delta$ -matter are represented by long-dashed curves. The horizontal dotted lines denote the upper bounds on $\Lambda_{1,4} = 800, 580$ obtained from Abbott et al. (2017a) and recent re-analysis Abbott et al. (2018) respectively (GW170817 event). The vertical range denotes joint constraints from NICER observations (PSR J0030+0451) & GW170817 event (Jiang et al. 2020) and another obtained implementing Bayesian analysis (Li et al. 2021b) for a $1.4 M_{\odot}$ NS. The various astrophysical constraints are similar as in fig.-2.

where $M_T = 2.73 - 2.78 M_{\odot}$. The masses of the two components are varied in $1.36 \leq M_1/M_{\odot} \leq 1.60$ (primary) and $1.17 \leq M_2/M_{\odot} \leq 1.36$ (secondary) ranges (Abbott et al. 2017a). From the left panel of fig.-6, it is observed that for pure nucleonic matter the NLW CDF model parametrization GM1 do not lie within the 90% probability contours of $\tilde{\Lambda} \sim 900$, although GM2 and GM3 do, while in case of DD CDF models, all the parametrizations lie inside these $\tilde{\Lambda} \sim 900$ contours. In the case of matter composition as NY , the tidal deformability is quite similar to the ones with pure nucleonic matter and hence not shown in fig.-6. In case of Δ -resonance admixed hypernuclear matter, for all the relevant EOSs Λ_1, Λ_2 falls well even within the $\tilde{\Lambda} \sim 720$ probability contour (obtained from recent re-analysis) as shown in the right panel of the figure. Table-3 provides the numerical estimates of various observational properties of different CDF models considering matter composition to be purely nucleonic, hypernuclear and Δ -resonance admixed hypernuclear matter.

Next we attempt to restrict radius of compact stars by evaluating $\tilde{\Lambda}$ with particular star combinations for both the events considering different parametrization models. For the event GW170817, we have taken $M_1 = 1.50 M_{\odot}$ and $M_2 = 1.24 M_{\odot}$ and for the event GW190425 we have taken $M_1 = 1.70 M_{\odot}$ and $M_2 = 1.59 M_{\odot}$ where, M_1, M_2 correspond to primary and secondary components respectively. We plot the values of $\tilde{\Lambda}$ with radius of the primary star for respective EOSs in fig.-7. Tight correlations between $\tilde{\Lambda}$ and

Table 4. Threshold densities denoted by n_u^Y (in units of n_0) for onset of hyperons in hypernuclear dense matter for various DD CDF models. $n_{1.4}^{c(Y)}$ represents the central number density for a $1.4M_\odot$ NS with hypernuclear matter composition. $\Lambda_{1.4}^N, \Lambda_{1.4}^{NY}$ are the dimensionless tidal deformability of a $1.4M_\odot$ NS with nucleonic and hypernuclear matter respectively.

| CDF Model | $n_{1.4}^{c(Y)} (n_0)$ | $n_u^Y (n_0)$ | $\Lambda_{1.4}^N / \Lambda_{1.4}^{NY}$ |
|-----------|------------------------|---------------|--|
| DD1 | 2.42 | 2.26 | 0.998 |
| DD2 | 2.40 | 2.25 | 0.999 |
| DD-ME1 | 2.33 | 2.23 | 0.999 |
| DD-ME2 | 2.25 | 2.21 | 0.998 |
| PKDD | 2.48 | 2.15 | 1.01 |
| DD-MEX | 2.13 | 2.15 | 1.00 |

$R(M_1)$ are given by the fits

$$\begin{aligned}\tilde{\Lambda}_{\text{fit}}^{\text{(GW170817)}} &= 7571 - 1423R(M_1) + 68.93(R(M_1))^2, \\ \tilde{\Lambda}_{\text{fit}}^{\text{(GW190425)}} &= 2638 - 501.2R(M_1) + 24.34(R(M_1))^2,\end{aligned}$$

with maximum deviations, $(|\tilde{\Lambda}_{\text{fit}} - \tilde{\Lambda}|/\tilde{\Lambda}) \sim 2.65\%, 7.45\%$, $\chi^2 = \sum_i^N [(\tilde{\Lambda}_i^i - \tilde{\Lambda}_i^{\text{fit}})^2 / \tilde{\Lambda}_i^i] = 4.16, 7.16$ with $N = 30$ EOS models and coefficients of determination, $\mathcal{R}^2 = 1 - SS_{\text{res}}/SS_{\text{total}} \sim 0.999, 0.996$ for GW170817, GW190425 event respectively. Here, $SS_{\text{res}} = \sum_i (\tilde{\Lambda}_i - \tilde{\Lambda}_i^{\text{fit}})^2$, $SS_{\text{total}} = \sum_i (\tilde{\Lambda}_i - \bar{\tilde{\Lambda}})^2$ are sum of squares of the residual errors and squared error of the mean line respectively. The point where the curves cross $\tilde{\Lambda}$ bounds corresponds to limits on primary component's radius and hence the EOSs. The figure shows that the upper bound on $\tilde{\Lambda} \sim 900$ results in radius ≤ 13.44 km, which excludes certain NLW models except for GM2 and GM3 EOSs. On the other hand, if we consider the upper bound on $\tilde{\Lambda} \sim 720$, the radius bound ≤ 12.98 km not only excludes all the NLW EOSs but also matter without Δ resonances with DD parameterizations. From the lower bound of $\tilde{\Lambda} \sim 400$, the lower bound on radius ≥ 11.89 km which excludes dense matter composed of only nucleons with DDF (DD type) parameterization. From the observation of GW190425, the upper bound on $\tilde{\Lambda} \sim 600$ provides the upper bound on the primary component's radius ≤ 15.00 km, which gives no limit on the EOSs. Similar to fig.-7, effective tidal deformability as a function of secondary component's radius in GW170817 and GW190425 events is shown in fig.-8. The correlation fits between $\tilde{\Lambda}$ and $R(M_2)$ are given by

$$\begin{aligned}\tilde{\Lambda}_{\text{fit}}^{\text{(GW170817)}} &= 6249 - 1251R(M_2) + 63.62(R(M_2))^2, \\ \tilde{\Lambda}_{\text{fit}}^{\text{(GW190425)}} &= 2783 - 527.5R(M_2) + 25.48(R(M_2))^2,\end{aligned}$$

with maximum deviations of $\sim 17.76\%, 19.49\%$, $\chi^2 = 54.49, 17.44$ and $\mathcal{R}^2 \sim 0.983, 0.988$ for GW170817 and GW190425 events respectively. The upper bounds on radius for the secondary components in GW170817 case are estimated to be 13.37 km ($\tilde{\Lambda} \sim 900$), 12.94 km ($\tilde{\Lambda} \sim 720$) while the lower bound is evaluated to be 11.99 km ($\tilde{\Lambda} \sim 400$). In case of GW190425 case, radius of the secondary component, $R_{1.59} \leq 14.99$ km ($\tilde{\Lambda} \sim 600$). From both the correlations it can be inferred that the radius bounds on NSs involved in GW events are approximately $12 \leq R_*/\text{km} \leq 13$ and $R_* \leq 15$ km in GW170817 and GW190425 events respectively.

Fig.-9 depicts the dimensionless tidal deformability parameter as a function of NS mass evaluated from the DD and NLW type models with matter composition to be nucleonic and Δ -commixed baryon octet. It is observed that among the NLW CDF models, GM2 and GM3 parameterizations fulfil the $\Lambda_{1.4} = 800$ upper bound (with N -matter), while they fail to satisfy the recent $\Lambda_{1.4} = 580$ bound. Other NLW parameterizations produce larger radii NSs and, as a result, are

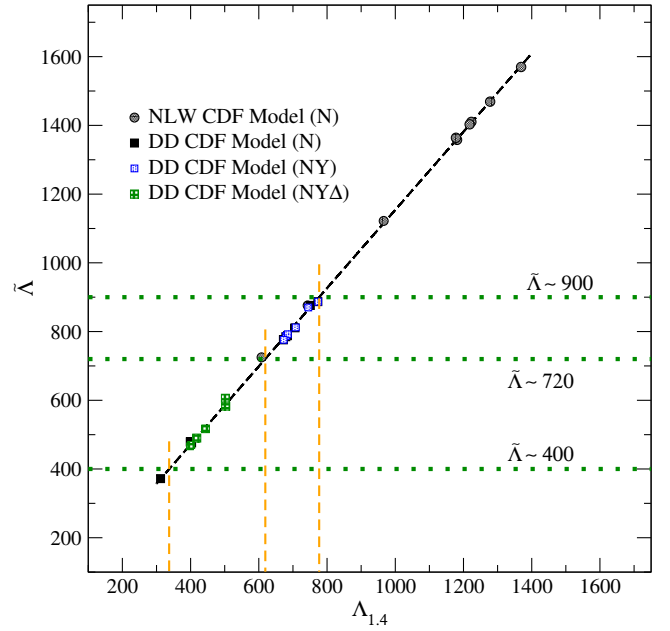


Figure 10. Correlation between weighted average tidal deformability and tidal deformability for $1.4 M_\odot$ NSs. The short-dashed line denotes the best fit for the EOS data sets. The bounds on $\tilde{\Lambda} \sim 900, 720$ (upper), 400 (lower) corresponding to GW170817 event are represented by the horizontal dotted lines similar to fig.-7. The vertical short-dashed lines mark the points where the linear fit intersects $\tilde{\Lambda}$ bounds. Parametrization models involved are similar as in fig.-7.

more inclined to be easily deformable since $\lambda \sim R^5$ (i.e. higher tidal deformability values). Hence no NLW model considered in this work satisfy the mass and tidal deformability constraints simultaneously. In the case of DD CDF models (with N -matter), all the models satisfy the upper bound constraint on $\Lambda_{1.4} = 800$. However, except TW99, DDV and DDF parameterizations none of them fulfil the upper bound ($\Lambda_{1.4} = 580$) obtained from re-analysis of GW170817 event data. No coupling parameter set considered in this work is seen to satisfy the more strict constraints of $\Lambda_{1.4} = 580$ and maximum mass simultaneously with pure nucleonic matter. Another joint constraint from NICER (PSR J0030+0451) and GW170817 data sets an upper bound on $\Lambda_{1.4} = 730$. Recent constraint on $\Lambda_{1.4}$ obtained from Bayesian analysis provides an upper bound of 686. DD CDF models (DD1, DD2, DD-ME1, DD-ME2) are observed to satisfy these criteria inclusive with the lower bound on M_{max} (see table-3 for numerical results). It should be noted, as evident from table-4 appearance of heavier baryons are inevitable in a $1.4 M_\odot$ star with all DD CDF parameterizations except DD-MEX.

Fig.-10 displays the tight correlation between weighted average $\tilde{\Lambda}$ and $\Lambda_{1.4}$ tidal deformability for GW170817 event data. In this case, we have considered $M_1 = 1.40 M_\odot$, $M_2 = 1.33 M_\odot$ with $\mathcal{M} = 1.1878 M_\odot$. The tight linear correlation between $\tilde{\Lambda}$ and $\Lambda_{1.4}$ is given by

$$\tilde{\Lambda}_{\text{fit}}^{\text{(GW170817)}} = 16.28 + 1.138\Lambda_{1.4},$$

with maximum deviation of $\sim 3.11\%$, $\chi^2 = 2.39$ and $\mathcal{R}^2 \sim 0.999$. The upper bounds on $\Lambda_{1.4}$ are deduced to be 777, 619 corresponding to $\tilde{\Lambda} \sim 900, 720$ respectively. While the lower bound on $\Lambda_{1.4}$ based on $\tilde{\Lambda} \sim 400$ (AT2017gfo) is estimated to be 337. The upper bound on $\tilde{\Lambda}$ favours the DD parameterizations as evident from fig.-10.

We have shown the dependence of Λ on compactness of the star

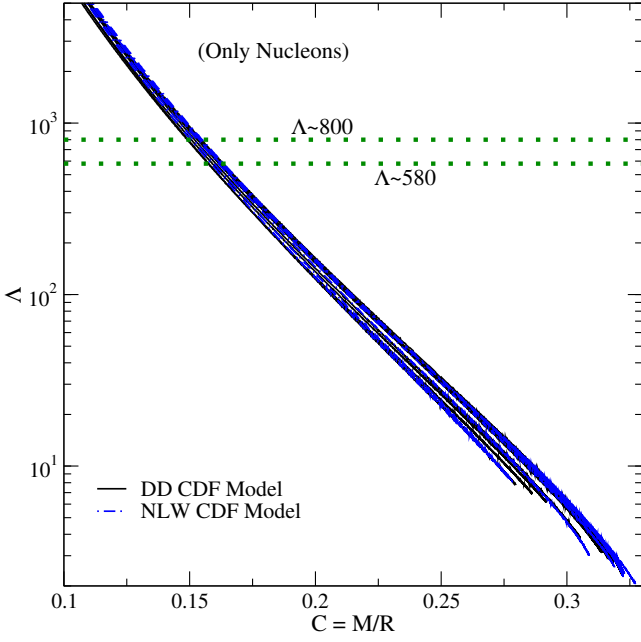


Figure 11. Dimensionless tidal deformability as a function of compactness parameter (C) for an isolated NS (with N -matter) for the CDF parametrizations implemented in this work. The bounds on $\Lambda \sim 800, 580$ corresponding to GW170817 event are represented by the horizontal dotted lines similar to fig.-9.

for different parametrizations (with N -matter) in fig.-11. From the figure, it is clear that the dependence of Λ on compactness is almost independent of EOSs. This relates with the result from Ref.-Maselli et al. (2013). Then in fig.-12, we plot the Λ for an isolated NS of mass $1.4M_{\odot}$ which shows a general trend with almost all EOSs. In order to find lower bound on the compactness parameter of a $1.4M_{\odot}$ NS ($C_{1.4}$), we compute the correlations between $\Lambda_{1.4}$ and $C_{1.4}$ as $\Lambda_{1.4}/10^4 = 2.094 - 22.67C_{1.4} + 62.2C_{1.4}^2$. The maximum deviation estimated is $\sim 11.94\%$ with $\chi^2 = 41.03$, \mathcal{R}^2 corresponding to 0.989. The stiffer NLW type parametrization models produce compact stars with larger mass and radius leading to higher tidal deformabilities. Obviously, these stiffer EOSs do not fulfil the upper limit of $\Lambda_{1.4} \leq 800$. Softer parametrizations GM2 and GM3 satisfy the upper limit of Λ . On the other hand, DD type parametrizations considered in this work generate compact stars with $\Lambda_{1.4} \leq 800$. Inclusion of Δ -resonances reduces $R_{1.4}$ resulting in increase of $C_{1.4}$ keeping Λ less than its upper limit. From fig.-12, it can be inferred that for a $1.4M_{\odot}$ NS, the lower bound in compactness is 0.153(0.154) corresponding to $\Lambda_{1.4} \sim 800(777)$ and it is 0.160(0.159) following the stringent upper bound of $\Lambda_{1.4} \sim 580(619)$. It also shows that the upper bound in compactness for a $1.4M_{\odot}$ NS is 0.173 following the lower bound $\Lambda_{1.4} \sim 337$. The points which lie away from the correlation fit are from GM2, GM3, PKDD coupling models. Based on the derived bounds of $C_{1.4}$, the range of $R_{1.4}$ is found to be 11.95 – 13.00 km ($C_{1.4} \sim 0.159 - 0.173$) and 11.95 – 13.42 km (0.154 – 0.173). The estimated bounds on $R_{1.4}$ satisfy the range $11.5 \leq R_{1.4}/\text{km} \leq 13.6$ as reported in Ref.-(Li & Steiner 2006) with the latter constrained from terrestrial experimental data.

In addition to heavier baryons, meson such as (anti)kaon condensations may also come into the picture with rising energy density towards the interior of NSs. Thapa & Sinha (2020); Thapa et al. (2021) reported that these meson condensations affect the lowering

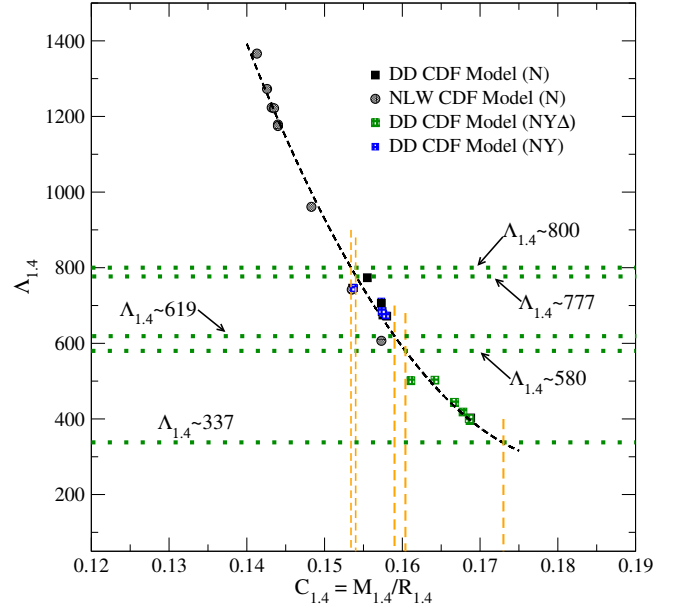


Figure 12. Correlation between tidal deformability and compactness parameter for $1.4M_{\odot}$ NSs. The short-dashed line denotes the best fit for the EOS data sets. The bounds on $\Lambda_{1.4}$ corresponding to GW170817 event are represented by the horizontal dotted lines similar to figs.-9,11 in addition to ones deduced from fig.-10. The vertical short-dashed lines mark the points where the quadratic fit intersects $\Lambda_{1.4}$ bounds. Parametrization models involved are similar as in fig.-7.

of maximum mass NS configurations and do not have any significant reduction in radii of $\sim 1.4M_{\odot}$ NSs compared to pure hadronic matter cases.

5 CONCLUSIONS AND OUTLOOK

The BNS mergers provide intriguing information to constrain various theoretical formulations of dense nuclear matter EOSs. In this work, we have analysed two schemes of coupling parametrizations and tried to constrain purely nucleonic, hypernuclear and Δ -baryon admixed hypernuclear matter EOSs within the CDF framework model via employing GW and other astrophysical observations.

Confronting the coupling parametrizations considered in this work with the recent bounds on nuclear saturation properties infers that the NLW parameter sets fail to satisfy these empirical ranges while DD coupling models (except PKDD) are seen to fulfil these bounds. In addition, imposing the lower limit of maximum mass constraint rules out the relatively softer EOSs viz. GM2, GM3 among NLW models and DDF, DDV, TW99 among DD CDF models. On the other hand, very stiff NLW EOSs, except GM1 fail to satisfy the measured radius range from observation of PSR J0030 + 0451. In the core of NSs, with enhanced matter density, the appearance of heavier baryons are inevitable. Their appearance softens the matter, excluding some more parametrization viz. DD1, DD2, PKDD among DD CDF models and only admissible NLW model parametrization GM1. Even with pure nucleonic matter, the parametrization GM1 is ruled out because it is not as soft as to provide $\tilde{\Lambda} \leq 900$ from GW170817 event. Hence, none of the parameter sets within NLW model considered in this work can satisfy all the observational constraints simultaneously. The upper bound on $\tilde{\Lambda} \leq 900$ allow all the parametrizations of DD CDF models, although the strict upper limit $\tilde{\Lambda} \leq 720$ does not allow any

parametrization with pure nuclear matter maintaining lower bound constraints of maximum mass. However, the appearance of heavier non-strange baryons allows all the DD CDF parametrizations to lie within the stringent upper limit.

The advent of heavier baryons (hyperons) leads to softening of EOSs, which in turn reduce the NS maximum masses values by $\sim 0.38 M_{\odot}$ than that of pure nucleonic cases. The effect on dimensionless tidal deformability ($\Lambda_{1.4}$) due to the incorporation of hyperons is very marginal. It can be seen that the central number densities of $1.4M_{\odot}$ NSs are quite close to the onset of hyperons. This attributes to the marginal changes in $\Lambda_{1.4}$. However, the appearance of Δ -resonances in dense matter is worthy of mentioning. From fig.-9, it can be seen that the value of $\Lambda_{1.4}$ lies above the stringent 580 upper bound for the stiffer DD CDF EOSs for pure nucleonic matter. With the advent of Δ -quartet, $\Lambda_{1.4}$ reduces sufficiently and moves below 580 for all stiff DD CDF parametrizations considered in this work. This relates with the results from Refs.-Li & Sedrakian (2019); Raduta (2021). Δ -baryon admixed hypernuclear NSs are observed to have smaller radius values in comparison to the NSs with only baryon octet particle spectrum (refer to table-3). This is due to the early onset of Δ^- baryon, which relatively softens the EOSs at lower densities.

Abbott et al. (2021) recently reported the observation of GWs from two NS-BH coalescences (GW200105 and GW200115). The masses of the NSs involved are deduced to be $1.9^{+0.3}_{-0.2} M_{\odot}$, $1.5^{+0.7}_{-0.3} M_{\odot}$ for the GW200105 and GW200115 events respectively. However, no constraints on tidal deformation of the secondary components have been reported. The coupling parametrizations considered in this work satisfy the NS mass constraints set by these recent GW events.

Based on the coupling data sets contemplated in this work and observed strict restrictions on $\tilde{\Lambda}$, a radius range of the NSs involved in GW170817 event is deduced to be around $12 \leq R_*/\text{km} \leq 13$ and that with GW190425 event's data is found to be $R_* \leq 15.00$ km. The lower bound on $\tilde{\Lambda}$ considered in this work is evaluated from the electromagnetic counterpart (kilonova) signal in GW170817 event. The strong correlation between weighted average $\tilde{\Lambda}$ and $\Lambda_{1.4}$ sets bounds as $337 \leq \Lambda_{1.4} \leq 619$ corresponding to $400 \leq \tilde{\Lambda} \leq 720$. Furthermore, similar analysis with strict bounds on $\Lambda_{1.4}$ translate to compactness parameter value of a $1.4 M_{\odot}$ NS to be in the range $0.159 \leq C_{1.4} \leq 0.173$. This yields $R_{1.4}$ in the range 11.95 – 13.00 km.

Another inference from the GW observational constraints is the possible existence of quark matter in the interior of NSs. Many works (Nandi & Char 2018; Gomes et al. 2019; Paschalidis et al. 2018; Mariani et al. 2019; Nandi & Pal 2021; Rather et al. 2021) reported hybrid star configurations consistent with the strict upper bounds on $\tilde{\Lambda}$, $\Lambda_{1.4}$ and massive NS observations. Since the knowledge regarding high-density quark matter is still inadequate, we could explore and constrain the parameter space of the functionals involved in describing the quark matter behaviour at such density regimes based on GW events and recent NICER data. Further analysis on the aspect is beyond the scope of this work and will be discussed in future studies.

ACKNOWLEDGEMENTS

The authors thank the anonymous referee for constructive comments that significantly contributed to enhancing the manuscript's quality. The authors acknowledge financial support from Science and Engineering Research Board, Department of Science and Technology, Government of India through Project No. EMR/2016/006577 and

Ministry of Education, Government of India. V.B.T and M.S are also thankful to Sarmistha Banik for fruitful discussions.

DATA AVAILABILITY

Data sharing not applicable to this article as no datasets were generated during the current study.

REFERENCES

- Abbott B. P., Abbott R., Abbott T. D., Acernese F., Ackley K., et al., 2017a, *PhRvL*, 119, 161101
- Abbott B. P., Abbott R., Adhikari R. X., Ananyeva A., Anderson S. B., et al., 2017b, *ApJL*, 848, L12
- Abbott B. P., Abbott R., Abbott T. D., Acernese F., Ackley K., et al., 2017c, *ApJL*, 848, L13
- Abbott B. P., Abbott R., Abbott T. D., Acernese F., Ackley K., et al., 2018, *PhRvL*, 121, 161101
- Abbott B. P., Abbott R., Abbott T. D., et al., 2019, *Phys. Rev. X*, 9, 011001
- Abbott B. P., et al., 2020a, *ApJ*, 892, L3
- Abbott R., et al., 2020b, *ApJ*, 896, L44
- Abbott R., et al., 2021, *ApJ*, 915, L5
- Akmal A., Pandharipande V. R., Ravenhall D. G., 1998, *Phys. Rev. C*, 58, 1804
- Antoniadis J., et al., 2013, *Science*, 340, 448
- Arzoumanian Z., et al., 2018, *ApJ Suppl.*, 235, 37
- Baillot d'Etivaux N., Guillot S., Margueron J., Webb N., Catelan M., Reisenegger A., 2019, *ApJ*, 887, 48
- Banik S., Bandyopadhyay D., 2001, *Phys. Rev. C*, 63, 035802
- Bao S. S., Shen H., 2014, *Phys. Rev. C*, 89, 045807
- Baym G., Pethick C., Sutherland P., 1971, *ApJ*, 170, 299
- Baym G., Hatsuda T., Kojo T., Powell P. D., Song Y., Takatsuka T., 2018, *Rep. Prog. Phys.*, 81, 056902
- Binnington T., Poisson E., 2009, *Phys. Rev. D*, 80, 084018
- Biswas B., 2021, arXiv e-prints, p. arXiv:2105.02886
- Boguta J., Bodmer A. R., 1977, *Nuclear Phys. A*, 292, 413
- Bombaci I., Drago A., Logoteta D., Pagliara G., Vidana I., 2020, arXiv e-prints, p. arXiv:2010.01509
- Bonanno L., Sedrakian A., 2012, *A&A*, 539, A16
- Cai B.-J., Fattoyev F. J., Li B.-A., Newton W. G., 2015, *Phys. Rev. C*, 92, 015802
- Carlson J., Gandolfi S., Pederiva F., Pieper S. C., Schiavilla R., Schmidt K. E., Wiringa R. B., 2015, *Reviews of Modern Physics*, 87, 1067
- Chatterjee D., Vidana I., 2016, *European Physical Journal A*, 52, 29
- Chen Y., Guo H., Liu Y., 2007, *Phys. Rev. C*, 75, 035806
- Colucci G., Sedrakian A., 2013, *Phys. Rev. C*, 87, 055806
- Cozma M. D., Tsang M. B., 2021, arXiv e-prints, p. arXiv:2101.08679
- Cromartie H. T., et al., 2020, *Nature Astronomy*, 4, 72
- Damour T., Nagar A., 2010, *Phys. Rev. D*, 81, 084016
- Demorest P. B., Pennucci T., Ransom S. M., Roberts M. S. E., Hessels J. W. T., 2010, *Nature*, 467, 1081
- Dexheimer V., Gomes R. O., Klöhn T., Han S., Salinas M., 2021, *Phys. Rev. C*, 103, 025808
- Douchin F., Haensel P., 2001, *A&A*, 380, 151
- Drago A., Lavagno A., Pagliara G., Pigato D., 2014, *Phys. Rev. C*, 90, 065809
- Fattoyev F. J., Horowitz C. J., Piekarewicz J., Reed B., 2020, *Phys. Rev. C*, 102, 065805
- Favata M., 2014, *Phys. Rev. Lett.*, 112, 101101
- Feliciello A., Nagae T., 2015, *Reports on Progress in Physics*, 78, 096301
- Flanagan E. E., Hinderer T., 2008, *Phys. Rev. D*, 77, 021502
- Fonseca E., et al., 2021, arXiv e-prints, p. arXiv:2104.00880
- Fortin M., Providência C., Raduta A. R., Gulminelli F., Zdunik J. L., Haensel P., Bejger M., 2016, *Phys. Rev. C*, 94, 035804
- Friedman E., Gal A., 2021, arXiv e-prints, p. arXiv:2104.00421
- Gal A., Hungerford E. V., Millener D. J., 2016, *Rev. Mod. Phys.*, 88, 035004

- Glendenning N. K., 1996, *Compact Stars*, (Springer-Verlag, New York, 2007), 2nd ed.
- Glendenning N. K., Moszkowski S. A., 1991a, *Phys. Rev. Lett.*, **67**, 2414
- Glendenning N. K., Moszkowski S. A., 1991b, *Phys. Rev. Lett.*, **67**, 2414
- Glendenning N. K., Schaffner-Bielich J., 1999, *Phys. Rev. C*, **60**, 025803
- Gomes R. O., Dexheimer V., Schramm S., Vasconcellos C. A. Z., 2015, *ApJ*, **808**, 8
- Gomes R. O., Char P., Schramm S., 2019, *ApJ*, **877**, 139
- Haensel P., Proszynski M., 1982, *ApJ*, **258**, 306
- Hinderer T., 2008, *The Astrophysical Journal*, **677**, 1216
- Hinderer T., Lackey B. D., Lang R. N., Read J. S., 2010, *Phys. Rev. D*, **81**, 123016
- Hofmann F., Keil C. M., Lense H., 2001, *Phys. Rev. C*, **64**, 025804
- Jiang J.-L., Tang S.-P., Wang Y.-Z., Fan Y.-Z., Wei D.-M., 2020, *The Astrophysical Journal*, **892**, 55
- Kanakis-Pegios A., Moustakidis C., 2020, *HNPS Advances in Nuclear Physics*, **27**, 95
- Klähn T., et al., 2006, *Phys. Rev. C*, **74**, 035802
- Koch J., Ohtsuka N., 1985, *Nuclear Physics A*, **435**, 765
- Kolomeitsev E., Maslov K., Voskresensky D., 2017, *Nuclear Physics A*, **961**, 106
- Kumar B., Biswal S. K., Patra S. K., 2017, *Phys. Rev. C*, **95**, 015801
- Lalazissis G. A., König J., Ring P., 1997, *Phys. Rev. C*, **55**, 540
- Lalazissis G. A., Nikšić T., Vretenar D., Ring P., 2005, *Phys. Rev. C*, **71**, 024312
- Lalazissis G., Karatzikos S., Fossion R., Arteaga D. P., Afanasjev A., Ring P., 2009, *Physics Letters B*, **671**, 36
- Landry P., Essick R., Chatziioannou K., 2020, *Phys. Rev. D*, **101**, 123007
- Lattimer J. M., Prakash M., 2016, *Phys. Rep.*, **621**, 127
- Li J. J., Sedrakian A., 2019, *ApJ*, **874**, L22
- Li B.-A., Steiner A. W., 2006, *Physics Letters B*, **642**, 436
- Li J. J., Long W. H., Sedrakian A., 2018a, *European Physical Journal A*, **54**, 133
- Li J. J., Sedrakian A., Weber F., 2018b, *Physics Letters B*, **783**, 234
- Li J. J., Sedrakian A., Weber F., 2018c, *Phys. Lett. B*, **783**, 234
- Li J. J., Sedrakian A., Alford M., 2020a, *Phys. Rev. D*, **101**, 063022
- Li J. J., Sedrakian A., Weber F., 2020b, *Physics Letters B*, **810**, 135812
- Li B.-A., Cai B.-J., Xie W.-J., Zhang N.-B., 2021a, arXiv e-prints, p. arXiv:2105.04629
- Li Y., Chen H., Wen D., Zhang J., 2021b, *European Physical Journal A*, **57**, 31
- Logoteta D., 2019, *Phys. Rev. C*, **100**, 045803
- Long W., Meng J., Giai N. V., Zhou S.-G., 2004, *Phys. Rev. C*, **69**, 034319
- Malik T., Alam N., Fortin M., Providência C., Agrawal B. K., Jha T. K., Kumar B., Patra S. K., 2018, *Phys. Rev. C*, **98**, 035804
- Malik T., Banik S., Bandyopadhyay D., 2021, *European Physical Journal Special Topics*,
- Mannarelli M., 2019, *Particles*, **2**, 411
- Mariani M., Orsaria M. G., Ranea-Sandoval I. F., Lugones G., 2019, *MNRAS*, **489**, 4261
- Maselli A., Cardoso V., Ferrari V., Gualtieri L., Pani P., 2013, *Phys. Rev. D*, **88**, 023007
- Miller M. C., et al., 2019, *ApJ*, **887**, L24
- Miller M. C., et al., 2021, arXiv e-prints, p. arXiv:2105.06979
- Mondal C., Agrawal B. K., De J. N., Samaddar S. K., Centelles M., Viñas X., 2017, *Phys. Rev. C*, **96**, 021302
- Most E. R., Papenfort L. J., Weih L. R., Rezzolla L., 2020, *MNRAS*, **499**, L82
- Motta T. F., Thomas A. W., Guichon P. A. M., 2020, *Physics Letters B*, **802**, 135266
- Nakamura S. X., Sato T., Lee T.-S. H., Szczerbinska B., Kubodera K., 2010, *Phys. Rev. C*, **81**, 035502
- Nandi R., Char P., 2018, *The Astrophysical Journal*, **857**, 12
- Nandi R., Pal S., 2021, *European Physical Journal Special Topics*,
- Nandi R., Char P., Pal S., 2019, *Phys. Rev. C*, **99**, 052802
- Nikšić T., Vretenar D., Finelli P., Ring P., 2002, *Phys. Rev. C*, **66**, 024306
- Oertel M., Providência C., Gulminelli F., Raduta A. R., 2015, *J. Phys. G*, **42**, 075202
- Oertel M., Hempel M., Klähn T., Typel S., 2017, *Reviews of Modern Physics*, **89**, 015007
- Pal S., Bandyopadhyay D., Greiner W., 2000, *Nuclear Phys. A*, **674**, 553
- Pang P. T. H., Tews I., Coughlin M. W., Bulla M., Van Den Broeck C., Dietrich T., 2021, arXiv e-prints, p. arXiv:2105.08688
- Paschalidis V., Yagi K., Alvarez-Castillo D., Blaschke D. B., Sedrakian A., 2018, *Phys. Rev. D*, **97**, 084038
- Prakash M., Bombaci I., Prakash M., Ellis P. J., Lattimer J. M., Knorren R., 1997, *Phys. Rep.*, **280**, 1
- Raaijmakers G., et al., 2021, arXiv e-prints, p. arXiv:2105.06981
- Radice D., Perego A., Zappa F., Bernuzzi S., 2018, *ApJL*, **852**, L29
- Raduta A. R., 2021, *Physics Letters B*, **814**, 136070
- Raduta A. R., Sedrakian A., Weber F., 2018, *MNRAS*, **475**, 4347
- Raithel C. A., Özel F., Psaltis D., 2018, *The Astrophysical Journal*, **857**, L23
- Rashdan M., 2001, *Phys. Rev. C*, **63**, 044303
- Rather I. A., Rahaman U., Imran M., Das H. C., Usmani A. A., Patra S. K., 2021, *Phys. Rev. C*, **103**, 055814
- Ribes P., Ramos A., Tolos L., Gonzalez-Boquera C., Centelles M., 2019, *ApJ*, **883**, 168
- Riley T. E., et al., 2019, *ApJ*, **887**, L21
- Riley T. E., et al., 2021, arXiv e-prints, p. arXiv:2105.06980
- Romani R. W., Kandel D., Filippenko A. V., Brink T. G., Zheng W., 2021, *ApJ*, **908**, L46
- Sahoo H. S., Mitra G., Mishra R., Panda P. K., Li B.-A., 2018, *Phys. Rev. C*, **98**, 045801
- Schaffner-Bielich J., Gal A., 2000, *Phys. Rev. C*, **62**, 034311
- Schaffner J., Dover C., Gal A., Greiner C., Millener D., Stocker H., 1994, *Annals of Physics*, **235**, 35
- Sedrakian A., 2007, *Progress in Particle and Nuclear Physics*, **58**, 168
- Sedrakian, Armen 2017, *EPJ Web Conf.*, **164**, 01009
- Sedrakian A., Weber F., Li J. J., 2020, *Phys. Rev. D*, **102**, 041301
- Sedrakian A., Li J.-J., Weber F., 2021, arXiv e-prints, p. arXiv:2105.14050
- Serot B. D., Walecka J. D., 1997, *International Journal of Modern Physics E*, **6**, 515
- Sharma M., Nagarajan M., Ring P., 1993, *Physics Letters B*, **312**, 377
- Somasundaram R., Margueron J., 2021, arXiv e-prints, p. arXiv:2104.13612
- Taninah A., Agbemava S., Afanasjev A., Ring P., 2020, *Physics Letters B*, **800**, 135065
- Tews I., Margueron J., Reddy S., 2018, *PhRvC*, **98**, 045804
- Tews I., Pang P. T. H., Dietrich T., Coughlin M. W., Antier S., Bulla M., Heinzel J., Issa L., 2021, *The Astrophysical Journal*, **908**, L1
- Thapa V. B., Sinha M., 2020, *Phys. Rev. D*, **102**, 123007
- Thapa V. B., Sinha M., Li J. J., Sedrakian A., 2020, *Particles*, **3**, 660
- Thapa V. B., Sinha M., Li J. J., Sedrakian A., 2021, *Phys. Rev. D*, **103**, 063004
- Tolos L., Fabbietti L., 2020, *Progress in Particle and Nuclear Physics*, **112**, 103770
- Tolos L., Centelles M., Ramos A., 2017, *Publ. Astron. Soc. Austral.*, **34**, e065
- Typel S., 2005, *Phys. Rev. C*, **71**, 064301
- Typel S., Alvear Terrero D., 2020, *Eur. Phys. J. A*, **56**, 160
- Typel S., Wolter H., 1999, *Nuclear Physics A*, **656**, 331
- Typel S., Röpke G., Klähn T., Blaschke D., Wolter H. H., 2010, *Phys. Rev. C*, **81**, 015803
- Vautherin D., Brink D. M., 1972, *Phys. Rev. C*, **5**, 626
- Walecka J. D., 1974, *Annals of Physics*, **83**, 491
- Weber F., 2017, *Pulsars as Astrophysical Laboratories for Nuclear and Particle Physics. Series in High Energy Physics, Cosmology and Gravitation*, CRC Press, <https://books.google.co.in/books?id=SSw2DwAAQBAJ>
- Wehrberger K., Bedau C., Beck F., 1989, *Nuclear Physics A*, **504**, 797
- Weissenborn S., Chatterjee D., Schaffner-Bielich J., 2012, *Nucl. Phys. A*, **881**, 62
- Yagi K., Yunes N., 2017, *Phys. Rep.*, **681**, 1
- Zhang N.-B., Li B.-A., 2021, arXiv e-prints, p. arXiv:2105.11031
- Zhu Z.-Y., Li A., Hu J.-N., Sagawa H., 2016, *Phys. Rev. C*, **94**, 045803
- Zimmerman J., Carson Z., Schumacher K., Steiner A. W., Yagi K., 2020, arXiv e-prints, p. arXiv:2002.03210